Light trapping and absorption optimization in certain thin-film photonic crystal architectures

Alongkarn Chutinan and Sajeev John

Department of Physics, University of Toronto, 60 St. George Street, Toronto, Ontario, Canada, M5S 1A7

We demonstrate two orders of magnitude enhancement of light absorption in certain thin-film photonic crystal (PC) architectures due to strong resonances arising from parallel interface refraction (PIR). This anomalous type of refraction is acutely negative and usually out of the plane of incidence. Over a wide range of frequencies, light impinging on idealized two-dimensional (2D) thin-film photonic crystals, over a cone of at least 20° in off-normal directions, couples to Bloch modes propagating nearly parallel to the thin-film–to–air interface. For realistic three-dimensional PC films of cubic symmetry, synthesized by photoelectrochemical etching, the PIR effect persists over a spectral range of at least 15% relative to the center frequency and within a cone of 50° of incident angles, normal to the film. This leads to anomalously long optical path lengths and long dwell times before the light beam exits the thin film. This near continuum of high-quality-factor optical resonances, associated with "transverse optical slow modes" in a spectral range of high electromagnetic density of states, can be much more effective for trapping and absorbing light than that of the previously reported longitudinal slow-group-velocity effects. The parallel interface refraction effect is general and can be found in specific spectral ranges of both 2D and 3D photonic crystals with cubic or other appropriate symmetries. In the presence of weak optical absorption within the PC backbone, energy conversion enhancement is interpreted using a simple temporal mode-coupling model. It is shown that absorption is optimized when the structural quality factor (in the absence of absorption) of the transverse optical slow modes is comparable to $\omega\tau_{abs}$, where ω is the optical frequency and τ_{abs} is the absorption time scale of the film material. Quantitative numerical results for light harvesting efficiency are obtained by finite-difference time-domain simulations of the electromagnetic wave field. It is shown that small amounts of fabrication-related structural disorder can introduce additional resonances and broaden existing resonances, thereby improving the overall harvesting of broadband wide-acceptance-angle light.

I. INTRODUCTION

A fundamental property of photonic band gap (PBG) materials is their ability to trap and localize light [1,2]. This same property is fundamental to applications involving the absorption and conversion of light to other forms of energy. This capability of PBG materials to localize light has yet to be fully exploited for solar-energy harvesting in thin films.

PBG materials [2,3] are a special class of photonic crystals, artificial optical materials in which the dielectric constant is periodically modulated on the scale of optical wavelengths. It has been suggested that a photon mobility edge [1] separating propagating from localized states in a bulk disordered dielectric medium would provide a spectral range for anomalously large optical absorption. The photonic band edge is the analog of a mobility edge in periodically ordered structures. In a semi-infinite photonic crystal, a crucial issue for "light harvesting" from an external source is the "coupling" of light into such slow-propagating or nonpropagating modes (and the reduction of reflection of light at the photonic-crystal–to–air interface).

In finite-thickness photonic crystal films, optical resonances that are symmetric with respect to the film boundaries lead to perfect transmission at the resonant frequency of each such mode. A crucial issue for light harvesting is the ratio of the "rate of coupling" (energy transfer) from the external source into and out of the cavity to the rate of absorption within the cavity. The optimum transfer of energy occurs when these two rates are matched. The coupling rate is in-versely proportional to the quality (Q) factor of the cavity, and the absorption rate is related to the imaginary part of the dielectric constant of the underlying material. For solar-energy harvesting, another crucial issue is the frequency bandwidth over which the required resonances occur and the range of incident angles over which efficient coupling to these cavity resonances is possible. In general, a broad range of frequencies and input angles is desirable. In this paper, we demonstrate that in suitably designed photonic crystals (PC's), strong resonances and efficient absorption of external plane waves for thin-film structures is possible within a 20° cone of incoming, off-normal angles and a range of frequencies. This occurs through the phenomenon of "parallel interface refraction" in PC thin films of appropriate point group symmetry.

Similar to electronic waves in semiconductors, the propagation of light in photonic crystals is represented by Bloch functions. Excitation of Bloch waves inside photonic crystals by external plane waves is accompanied by diffraction or refractionlike phenomena. In a frequency range near photonic band edges, effective refractive indices (defined by Snell's law) can become smaller than 1 or even negative. Such anomalous refraction phenomena have attracted broad interest. Experimental studies show that effective refractive indices become very dispersive near photonic band edges [4]. The so-called superprism phenomenon [5] (and its counterpart, the self-collimation effect [6]), where the angle of refraction inside photonic crystals is extremely sensitive (or insensitive) to the angle of incidence, utilizes anomalously dispersive properties of Bloch modes near the photonic band

gaps. Theoretical analysis reveals a mechanism of negative refraction in photonic crystals [7]. This suggests flat lenses with resolution beyond the diffraction limit [8]. In three-dimensional (3D) photonic crystals, the possibility of refraction out of the plane of incidence has been noted [9].

Previous literature on the enhancement of absorption in thin-film structures has focused on geometrical optics concepts [10]. A variety of light scattering surfaces ranging from random to ordered have been employed to scatter light into preferred directions inside the thin film (avoiding direct transmission through the film), with the aim of increasing the total path length (and dwell time) of light inside the thin film. The total absorption increases exponentially with the path length. For a uniform free-standing film of refractive index n and thickness d (in the x direction), a regularly spaced (in frequency) sequence of Fabry-Pérot resonances is expected when $nk_{0x}d = m\pi$ ($m = 1, 2, 3, \ldots$) where k_{0x} is the longitudinal component of the vacuum wave vector $k_0 = 2\pi/\lambda_0$. If the surface of this film is structured or randomized, these resonances may be broadened and their spectral positions randomized to provide a broader coverage of the desired spectral range. However, the average spectral density of these resonances remains the same as in the perfectly uniform film. When the film thickness is large compared to the vacuum wavelength λ_0, this provides absorption enhancement at specific resonant frequencies and specific incident angles.

A largely unexplored area consists of materials with dielectric features on the order of the optical wavelength (wave optics regime) with total thickness of only several wavelengths. In this situation a full vectorial wave analysis including effects such as partial reflection at dielectric interfaces and wave interferences is essential. In this paper, we demonstrate that, in the wave optics regime, a very high spectral density of high-quality resonances can be engineered over a desired spectral band. This occurs through periodic microstructuring of the thin film on a scale comparable to the optical wavelength. This takes the form of a continuum of strong resonances, associated with an elevated electromagnetic density of states. Moreover, the resonances can couple efficiently to incident plane waves impinging on the thin film from a broad range of angles. This enables greater overall absorption of light over a specified frequency range than conventional enhancement mechanisms based on geometrical ray optics. Optical phenomena such as light incident on an absorbing microstructured film require direct solution of Maxwell's equations. Certain features can also be modeled analytically by the mode-coupling theory [11].

It has long been realized that slow-group-velocity effects in photonic crystals can give rise to enhancement of gain or absorption. In one-dimensional photonic crystals, the slow group velocity at the band edges increases the interaction time between atoms and radiation field, leading to enhancement of stimulated emission [12]. In systems with higher dimensionality such as 2D or 3D photonic crystals, there exists another type of slow-group-velocity band that is absent in 1D systems. These arise from flat photonic bands that exist (the so-called group-velocity anomaly) even in the case of small dielectric contrast. Sakoda [13] demonstrated, in finite size PC's, that these flat bands enhance gain more efficiently than their 1D counterparts. Generally, slow-group-

velocity effects correspond to strong resonant modes. The resulting enhancement of gain or absorption can be interpreted using a high-Q cavity coupling analogy. In earlier studies [12,13], light incident normal to the photonic crystal/air interface was considered. In this paper, we demonstrate that light incident over a broad cone of off-normal directions exhibits the phenomenon of *parallel interface refraction* (PIR). This provides a frequency band of higher-quality resonances than previously reported slow-group-velocity effects. Furthermore, we demonstrate the possibility of strong enhancement of net optical absorption (integrated over finite frequency bands and incident angles) in thin-film photonic crystals using PIR, with practical value for light harvesting in solar cells.

The paper is organized as follows. In Sec. II, we review refraction and diffraction phenomena in photonic crystals and delineate specific architectural and photonic band structure criteria for realizing the PIR effect. Using finite-difference time-domain (FDTD) simulations, we demonstrate strong coupling resonances in 2D photonic crystal thin films arising from PIR. In Sec. III, we present a simplified model for coupling resonances and suggest optimal parameters for absorption enhancement based on the temporal mode-coupling theory. Detailed numerical results for absorption of light incident from various angles at various frequencies are presented in Sec. IV. The effects of structural disorder on the total absorption spectrum are presented in Sec. V. Finally, in Sec. VI, we demonstrate the PIR effect and concomitant absorption anomaly in 3D photonic crystal thin films with a simple cubic lattice symmetry.

II. PARALLEL INTERFACE REFRACTION

A fundamental analysis of refraction and diffraction at photonic crystal interfaces has been presented by Notomi [7]. A light beam incident from one uniform medium to another uniform medium follows Snell's law of refraction, expressed as $n_1 \sin(\theta_1) = n_2 \sin(\theta_2)$. Here, n_1 and n_2 are refractive indices of two uniform media and θ_1 and θ_2 are the angles of incidence and refraction, respectively. In order to generalize this law to periodically ordered microstructures, it is useful to interpret this as the phase-matching continuity condition for wave fronts traversing the interface. This is equivalent to the conservation of the lateral wave vector of the incident and refracted waves.

Consider light incident from air onto a thin slab of photonic crystal. After reflection and refraction at the first interface, some light is transmitted to air on the other side of the PC slab. In the first step, the incident plane wave excites Bloch mode(s) inside PC's. The internal wave is composed of an infinite series of plane wave components whose wave vectors differ by reciprocal lattice vectors of the PC. The phase-matching continuity condition requires that only the Bloch mode(s) consisting of a plane wave component with the same lateral wave vector as the incident lateral wave vector can be excited. In the final step, each of the internal plane wave components can excite a transmitted plane wave with the same lateral wave vector. By lateral momentum conservation, an infinite series of plane waves can be ex-

cited. Conservation of energy across the interface then restricts the number of transmitted waves by requiring that those with a lateral wave vector larger than the wave vector of the incident plane wave be evanescent. The actual number of diffracted waves depends on the relative scale between the wavelength of incident light and the lattice constant of PC's. The shorter the incident wavelength, the larger the number of diffracted waves. Explicitly, for an incident plane wave of wave vector $\vec{k}$, there are transmitted plane waves with all wave vectors $\vec{K}$, possessing a lateral wave vector $\vec{K}_\parallel \equiv \vec{k}_\parallel + \vec{G}_\parallel$, that satisfy $|\vec{K}| = |\vec{k}|$. Here, $\vec{k}_\parallel$ and $\vec{G}_\parallel$ are the parallel-to-the-interface components of the incident wave vector and any PC reciprocal lattice vector, respectively. For the zeroth-order diffraction, the corresponding $\vec{G}_\parallel$ is equal to $\vec{0}$ and the outgoing wave propagates in the same direction as the incident wave. However, in the case of negative-order diffraction, the transmitted waves may travel toward the opposite side of the surface normal line compared to the incident wave. Both refraction and diffraction phenomena are thereby described in a unified manner.

The refraction of light within the PC slab (before transmission to air on the other side) likewise presents a rich variety of interesting possibilities. The incident plane wave with a lateral wave vector $\vec{k}_\parallel$ can excite any Bloch modes with the same lateral Bloch vector at the same frequency inside photonic crystals. As pointed out by Notomi [7], in the case that refractive index modulation in PC's is very weak, one may associate different plane wave components of the Bloch mode with different orders of diffraction, e.g., zeroth, positive, and negative orders. However, in the case of strong refractive index modulation, especially in a high-frequency regime, a very large number of plane wave components become significant for composition of the Bloch mode. In this case, association of the different plane wave components of the Bloch mode with different orders of diffraction is less useful. Nevertheless, the analogy with the case of weak index modulation facilitates interpretation of *negative refraction*, in certain PC's, as negative first-order diffraction, where the zeroth-order diffraction is forbidden by the PBG. The direction of energy flow within the PC slab defines the overall optical path length taken by photons before they are transmitted. The optical path length together with the group velocity determines the overall dwell time of light within the slab. In the presence of a small absorption coefficient for the PC, these propagation characteristics are preserved and the dwell time determines the net absorption of light within the film. For light harvesting from a broadband source, it is highly desirable to achieve the longest possible dwell times for the maximum range of incoming light, impinging from different directions and covering the desired frequency range.

For concreteness, we consider a 2D photonic crystal consisting of a square lattice of dielectric rods in an air background as depicted in Fig. 1(a). The radius of the dielectric rods is 0.16a, where a is the lattice constant. The dielectric constant is assumed to be 11.9, corresponding to that of silicon at 1.5 μm wavelength. The corresponding band diagram for the E polarization (electric field perpendicular to the paper plane) is shown in Fig. 1(b). First, we assume a photonic
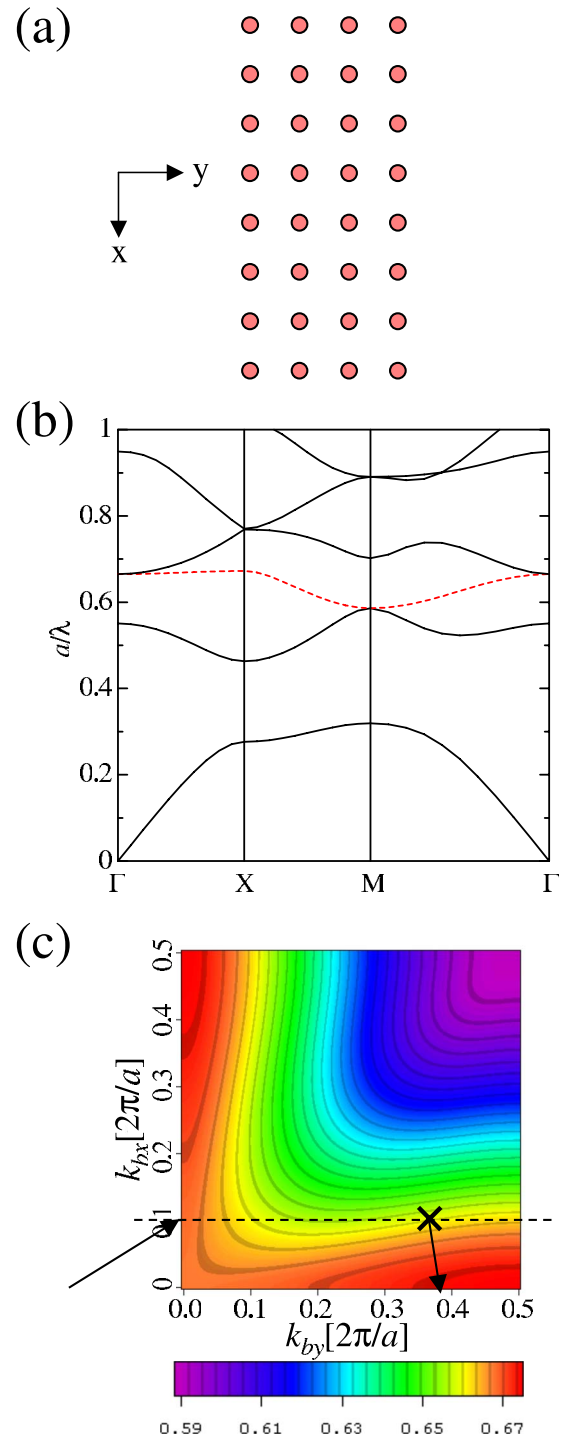

FIG. 1. (Color online) (a) Schematic of a 2D photonic crystal consisting a square lattice of dielectric rods in an air background. The photonic crystal/air interfaces are parallel to the Γ-X direction. (b) Band diagram for the square lattice photonic crystal. The dielectric constant and radius for circular rods are 11.9 and 0.16a, respectively. The third band is marked by the broken red (dark gray) line. (c) Contour plot of the eigenfrequency of the third band for the first Brillouin zone. The left arrow shows the wave vector of the incident plane wave. The broken line indicates eigenmodes with $k_{bx} = 0.1(2\pi/a)$. The right arrow indicates the direction of propagation of the Bloch mode $\vec{k}_b = (0.1, 0.36)(2\pi/a)$.

crystal structure with infinite size in the lateral direction and semi-infinite in depth. The photonic crystal/air interface is parallel to the Γ-X direction [as shown in Fig. 1(a)]. We focus on the third band [marked by the broken red (dark gray) line in Fig. 1(b)]. The isofrequency contours of the eigenfrequency of the third band are plotted in Fig. 1(c) for the first Brillouin zone. Consider, for example, a plane wave incident from air with a normalized frequency $a/\lambda = 0.658$ and an incident angle $\theta = 8.7°$. This is equivalent to a lateral wave vector of $k_x = 0.1(2\pi/a)$. Bloch modes inside photonic crystals that can be excited by this plane wave must also possess lateral Bloch vector k_{bx} equal to $0.1(2\pi/a)$ and the same frequency $a/\lambda = 0.658$. By looking at the isofrequency plot in Fig. 1(c), we find two modes [$k_{by} = 0.09(2\pi/a)$ and $0.36(2\pi/a)$] that match with the above conditions. For one of the two modes (marked by X), the Bloch vector is equal to $(0.1, 0.36)(2\pi/a)$. The direction of propagation of this mode is determined by its group velocity, which is normal to the isofrequency line at that Bloch vector. This is shown by the right arrow in Fig. 1(c), indicating sharply negative refraction. The propagation direction of the excited Bloch wave is nearly parallel to the photonic crystal/air interface. {The Bloch mode at the other intersection point [$k_{by} = 0.09(2\pi/a)$] is not excited due to its backward group velocity but its symmetric counterpart at $k_{by} = -0.09(2\pi/a)$ may be excited instead. However, this mode is not relevant to the parallel to interface resonance effect.}

In a photonic crystal with finite thickness, a Fabry-Pérot resonant condition further limits the number of Bloch modes that can exist inside the thin-film photonic crystal (see details in Appendix A). For a thin-film photonic crystal that supports the Bloch mode shown by X in Fig. 1(c), it is expected that light will spend a very long time propagating inside the photonic crystal before it exits the structure. These can equivalently be regarded as very high-quality- (Q-) factor resonant modes. Unlike the discrete resonances found in small dielectric cavities, the PC film exhibits a continuum of high-Q resonances that can be accessed over a band of frequencies and a range of incident angles. From the relative flatness of the iso-frequency contour near the point X [see Fig. 1(c)], the angle of refraction (defined by the direction of energy flow within the PC) remains relatively constant over a range of incident directions. We call this phenomenon parallel interface refraction.

As a result of the continuity of the isofrequency lines (2D) or surfaces (3D), it is possible to find single isolated points in the Brillouin zone from almost any band that yield PIR. For example, in the first band of the structure depicted in Fig. 1, the points along the Brillouin zone boundary exhibit group velocity vectors pointing exactly to the lateral direction. One of them is indicated by an X in Fig. 2. It is tempting to suggest that strong resonant optical modes can be found in *any* band of *any* photonic crystal. However, such resonant Bloch modes with a group velocity pointing exactly to the lateral direction cannot be excited due to their infinite quality factor. Instead, Bloch modes with a group velocity pointing slightly off the lateral direction are required for very strong, yet accessible, resonances. In Fig. 2, a Bloch mode at the position slightly to the left of X [e.g., $k_{by} = 0.49(2\pi/a)$] satisfies the above requirement. In a photonic crystal of finite
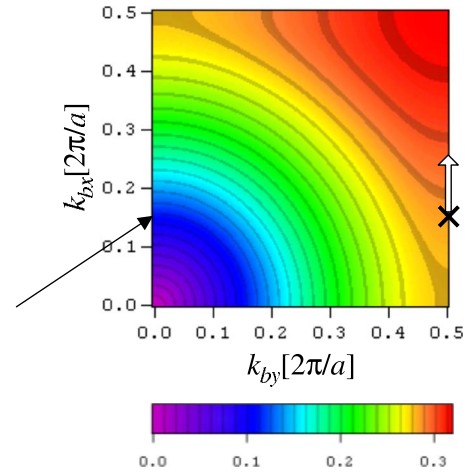

FIG. 2. (Color online) Contour plot of the eigenfrequency of the first band for a photonic crystal with the same structural parameters as in Fig. 1. The point indicated by X exhibits a group velocity vector pointing exactly to the lateral direction.

thickness L, the wave vector within the slab is attributed an uncertainty $\Delta k_{by} \sim 1/L$. Unless PIR persists over a range of wave vectors larger than its uncertainty, the effect is not robust. Indeed, the Fabry-Pérot condition for photonic crystal slabs (see Appendix A) reveals that a thickness of at least 50 unit cells is required for a photonic crystal slab to exhibit this PIR Bloch mode. In order to realize robust PIR in thin-film photonic crystals (with a very small number of unit cells, i.e., 2–3 unit cells in thickness), it is necessary to find isofrequency lines that are "flat," i.e., with normal vectors pointing nearly laterally over a broad range of Bloch vectors in the Brillouin zone. In 2D systems, we find that the square lattice is a better candidate than the triangular lattice since the latter tends to possess "round" isofrequency contours. Similar arguments apply for 3D systems where the simple cubic lattice is very well suited.

It is well known [13] that slow-group-velocity modes with Bloch vector normal to the interface can also serve as high-Q cavity modes. However, such "longitudinal" slow modes are not as effective as "transverse" slow modes (associated with PIR) in the harvesting of light. Here, we use FDTD simulation to compare the two resonance mechanisms. More detailed numerical results are presented in later sections. The second and fourth bands of the square lattice photonic crystals, shown in Fig. 1(b), exhibit flat dispersion along the Γ-X direction. Assuming a thickness of four unit cells, a transmission spectrum for a normally incident plane wave is shown in Fig. 3(a). Note that plane waves at exactly normal incidence do not couple to the third band due to the antisymmetric nature of its electric field distribution. From the transmission peak widths, it is apparent that the Q factors of resonant modes are larger for the second band ($a/\lambda \sim 0.48 - 0.54$) and the lower part of the fourth band ($a/\lambda \sim 0.66 - 0.69$) than for the first band ($a/\lambda \sim 0 - 0.26$).

Next, we calculate the transmission spectrum for an incident plane wave with a certain lateral wave vector k_x. Shown as a solid line in Fig. 3(b) is the transmission spectrum for $k_x = 0.2(2\pi/a)$. For off-normal incidence there is coupling to both band 3 and band 4. The spectrum for normal incidence
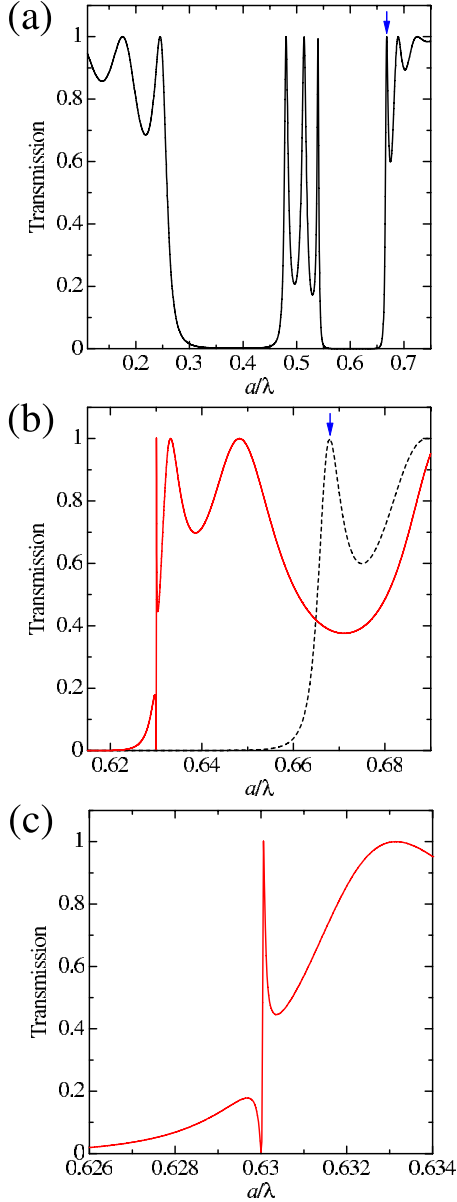
FIG. 3. (Color online) Transmission spectra calculated by 2D FDTD for a square lattice photonic crystal with thickness of four unit cells. (a) Incident plane wave is normal to the photonic crystal surface. (b) Incident plane wave possesses lateral wave vector k_x = $0.2(2\pi/a)$ (solid line). A transmission spectrum for normal incidence (broken line) is also overlaid for comparison. For reference, arrows indicating the same resonant mode at a/λ=0.668 for the normal incidence are shown in (a) and (b). (c) Details of the Fano line shape shown in (b).

(broken line) is also overlaid for comparison. Clearly, the off-normal incidence case further exhibits a remarkably sharp linewidth at a/λ=0.63 (corresponding to a larger Q factor), compared to the normal incidence case of the flat bands. Since only band 3 exists [see Fig. 1(b)] in the frequency range $a/\lambda \sim 0.60$–0.659, this suggests that the high-Q resonance is due to PIR from band 3. A simple argument for the position of Fabry-Pérot resonances in finite-thickness photonic crystals further suggests that the unusual sharp peak at a/λ=0.63 is indeed due to the coincidence of
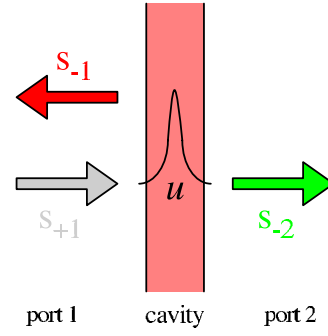

FIG. 4. (Color online) Schematic showing a cavity with two symmetric ports.

PIR with the Fabry-Pérot condition k_{by}=$(3/4)(\pi/a)$ for a PC film of thickness d=$4a$. In fact, both the frequency position and the linewidth of all the resonant peaks in Fig. 3(b) agree well with simple arguments for Fabry-Pérot resonances at k_{by}=$(3/4,2/4,1/4)(\pi/a)$ for the four-unit-cell-thick film. The detailed comparison is presented in Appendix A. We note that the off-normal incidence spectrum in Fig. 3(b) displays a Fano line shape [14,15]. This occurs whenever there exist two cavity modes that are near to each other in frequency but possess greatly different Q factors. In our case, there is interaction between the high-Q (PIR) mode at a/λ =0.63 and the neighboring finite-thickness slab resonance at a/λ=0.633 14 [k_{by}=$\pi/(2a)$]. Interference between the two modes results in the Fano line shape [16]. Figure 3(c) shows details of the Fano line shape at a/λ=0.63.

III. RESONANT ENHANCEMENT OF ABSORPTION

In a finite-size photonic crystal, the sample boundaries themselves provide a resonant cavity. It is tempting to argue that the slower the group velocity (or, equivalently, the larger the Q factor of the cavity), the longer the light will be trapped inside the cavity, and more absorption of light from an external source can be obtained. This argument is inaccurate. In fact, if the high Q factor makes it difficult for light to escape from the cavity, it necessarily means that it is also difficult for light to enter the cavity. As a result, for a given rate of absorption or gain, there exists an optimal Q factor yielding maximal net absorption or gain. First, we consider the case of absorption. The Q factor is a measure of the rate at which light in an eigenmode escapes from the cavity. It is defined by the equation

$$E(t) = E(0)e^{-t/\tau} \equiv E(0)e^{-(\omega_0 t)/Q}, \tag{1}$$

where E, ω_0, and τ are the energy, the angular frequency, and the decay time of the eigenmode, respectively. For an absorbing cavity with perfect mirrors, the energy in the eigenmode also decays exponentially with time. The decay time and Q factor for absorption are defined in a similar way. We denote the decay times for cavity and absorption as τ_{cav} and τ_{abs}, respectively, and the Q factors for cavity and absorption as $Q_{cav} \equiv \omega_0 \tau_{cav}$ and $Q_{abs} \equiv \omega_0 \tau_{abs}$, respectively.

For a specific example, we assume a cavity with only two symmetric ports (see Fig. 4), labeled 1 and 2, and no addi-
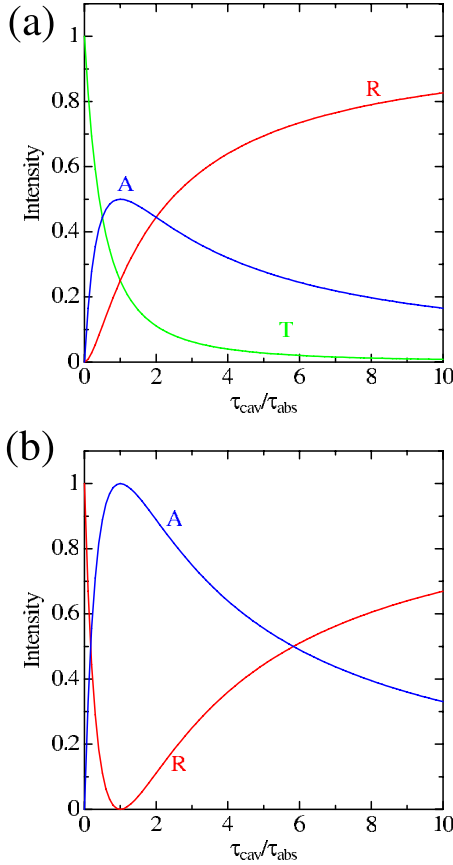
FIG. 5. (Color online) Transmission, reflection, and absorption coefficients as functions of the ratio $x \equiv \tau_{cav}/\tau_{abs}$ for (a) a cavity with two symmetric ports ($\tau_1 = \tau_2$) and (b) a cavity with two non-symmetric ports ($\tau_2 = \infty$). Note that the transmission coefficient is always zero in this case.

tional radiation losses. The cavity supports a single resonant frequency ω_0. First, we discuss the main results qualitatively. A detailed analysis using mode-coupling theory [11] is presented afterward. A maximal absorption of 50% of the incident light intensity is obtained at the resonant frequency when $Q_{cav} = Q_{abs}$. This maximal absorption can be understood as follows. When $Q_{abs} \gg Q_{cav}$, the cavity absorbs very little light. At the resonant frequency there is minimal reflection [see Fig. 5(a)]. Transmission is unity on resonance when there is no absorption ($Q_{abs} = \infty$). On the other hand, when $Q_{cav} \gg Q_{abs}$, it is more difficult for light to enter the cavity. The resulting increase in reflection leads to low absorption once again. Assuming that net absorption is a continuous function of Q_{cav} and Q_{abs}, a local maximum in absorption is expected when both quality factors are comparable.

In the case of a resonant cavity with gain, similar arguments apply. The maximal gain is obtained when $Q_{cav} = |Q_{gain}|$. Note that, for gain, the absorption quality factor is negative. When $|Q_{gain}| \gg Q_{cav}$, light passes through the cavity with minimal amplification and when $Q_{cav} \gg |Q_{gain}|$, light cannot enter the cavity but instead gets reflected.

A more quantitative treatment of net absorption in the cavity follows from mode-coupling theory [17]. In Fig. 4, the complex amplitude of the cavity mode is denoted by $u(t)$ and $u^*(t)u(t)$ gives the total energy inside the cavity. An incom-

ing wave on port 1, an outgoing wave on port 1, and an outgoing wave on port 2 are denoted by $s_{+1}(t)$, $s_{-1}(t)$, and $s_{-2}(t)$, respectively. The squared magnitude of these amplitudes is equal to the power (energy per unit time) approaching or leaving one of the film surfaces. We assume a cavity resonant frequency of ω_0, a cavity decay time of τ_{cav}, and an absorption decay time of τ_{abs}. The equation of motion for $u(t)$ is then assumed to be in the following form:

$$\frac{du(t)}{dt} = \left(i\omega_0 - \frac{1}{2\tau_{cav}} - \frac{1}{2\tau_{abs}} \right) u(t) + \kappa s_{+1}(t), \quad (2)$$

where κ is a coupling coefficient [with units of $1/\sqrt{time}$] from port 1 or 2 to the cavity. In this equation, all leakage into channels s_{-1} and s_{-2} is described by the single parameter $1/(2\tau_{cav})$. The value of κ is specified later to satisfy the conservation of energy. Notice that in Eq. (2) the amplitude decay time is twice the energy decay time defined in Eq. (1). The complex wave amplitude leaving port 1 consists of the 180° phase-shifted reflection of the incoming wave and a decay from the cavity amplitude with coupling coefficient d [with units of $1/\sqrt{time}$], given by $s_{-1} = -s_{+1} + du$. Similarly, the complex wave amplitude leaving port 2 is given by $s_{-2} = du$. Finally, the absorbed energy per unit time in the cavity is given by $|u|^2/\tau_{abs}$. Note that the amplitude coupling coefficient from the cavity to s_{-1} and s_{-2} is the same due to the assumed symmetry in the cavity mode. The conservation of energy

$$\frac{d|u(t)|^2}{dt} = |s_{+1}|^2 - |s_{-1}|^2 - |s_{-2}|^2 - \frac{|u|^2}{\tau_{abs}} \quad (3)$$

requires that $d = \kappa^*$, and that $|\kappa|^2 = 1/(2\tau_{cav})$. This can be confirmed by calculating $u^*(du/dt) + u(du^*/dt)$ using Eq. (2), comparing with Eq. (3), and eliminating s_{-1} and s_{-2} in favor of u and s_{+1}. For an incident continuous wave $s_{+1} = e^{i\omega t}$, the steady state solution ($t \to \infty$) of Eq. (2) yields the amplitude of the cavity mode:

$$u = \frac{\sqrt{1/2\tau_{cav}}}{i(\omega - \omega_0) + 1/2\tau_{cav} + 1/2\tau_{abs}} s_{+1}. \quad (4)$$

Using u from Eq. (4), we obtain the transmission and reflection amplitudes as follows:

$$\frac{s_{-1}}{s_{+1}} \equiv r = -1 + \frac{1/2\tau_{cav}}{i(\omega - \omega_0) + 1/2\tau_{cav} + 1/2\tau_{abs}}, \quad (5)$$

$$\frac{s_{-2}}{s_{+1}} \equiv t = \frac{1/2\tau_{cav}}{i(\omega - \omega_0) + 1/2\tau_{cav} + 1/2\tau_{abs}}. \quad (6)$$

At the resonant frequency, the transmission coefficient $T \equiv |t|^2$, reflection coefficient $R \equiv |r|^2$, and absorption coefficient $A \equiv 1 - T - R$ can be written as functions of $x \equiv \tau_{cav}/\tau_{abs}$ as follows:

$$T = \frac{1}{(1+x)^2}, \quad R = \frac{x^2}{(1+x)^2}, \quad A = \frac{2x}{(1+x)^2}. \quad (7)$$

These coefficients are plotted in Fig. 5(a). Clearly, the maximum absorption of 50% occurs when $\tau_{cav} = \tau_{abs}$. In Appendix B, we compare the results of mode-coupling theory with an

exact solution of Maxwell's equations for the case of Fabry-Pérot resonances in a 1D system to examine the range of validity of such a mode-coupling model. Our mode-coupling model result is derived for a cavity with a single resonant mode. For a cavity with more than one resonant mode, interplay between different resonant modes enables more than 50% absorption at certain frequencies.

The above model is based on a free-standing absorbing slab with symmetric ports. In practice, the absorbing film is placed on substrate or a reflecting back mirror, leading to asymmetry between the ports. It is straightforward to extend the above model to the asymmetric port case by replacing an inverse of the cavity decay time τ_{cav} (which describes a total cavity leakage) with the sum of inverse of the cavity decay time into port 1, τ_1, and port 2, τ_2. Equation (2) can then be rewritten as

$$\frac{du(t)}{dt} = \left(i\omega_0 - \frac{1}{2\tau_1} - \frac{1}{2\tau_2} - \frac{1}{2\tau_{\mathrm{abs}}}\right)u(t) + \kappa s_{+1}(t). \quad (8)$$

Consequently, the complex wave amplitudes leaving port 1 and port 2 are given by $s_{-1}=-s_{+1}+d_1 u$ and $s_{-2}=d_2 u$, respectively. Here, d_1 and d_2 are the coupling coefficients from the cavity to port 1 and port 2, respectively. Equation (8) is solved using a similar approach to that above. Finally, the transmission coefficient T, reflection coefficient R, and absorption coefficient $A \equiv 1-T-R$ can be written as functions of $1/\tau_1$, $1/\tau_2$, and $1/\tau_{\mathrm{abs}}$ as follows:

$$T = \frac{4\dfrac{1}{\tau_1}\dfrac{1}{\tau_2}}{\left(\dfrac{1}{\tau_1}+\dfrac{1}{\tau_2}+\dfrac{1}{\tau_{\mathrm{abs}}}\right)^2},$$

$$R = \frac{\left(-\dfrac{1}{\tau_1}+\dfrac{1}{\tau_2}+\dfrac{1}{\tau_{\mathrm{abs}}}\right)^2}{\left(\dfrac{1}{\tau_1}+\dfrac{1}{\tau_2}+\dfrac{1}{\tau_{\mathrm{abs}}}\right)^2},$$

$$A = \frac{4\dfrac{1}{\tau_1}\dfrac{1}{\tau_{\mathrm{abs}}}}{\left(\dfrac{1}{\tau_1}+\dfrac{1}{\tau_2}+\dfrac{1}{\tau_{\mathrm{abs}}}\right)^2}. \quad (9)$$

For comparison with the symmetric port case, in the following we rewrite T, R, and A as functions of $x \equiv \tau_{\mathrm{cav}}/\tau_{\mathrm{abs}}$ and $y \equiv \tau_1/\tau_2$, where $\tau_{\mathrm{cav}}=(1/\tau_1+1/\tau_2)^{-1}$:

$$T = \frac{4y}{(1+y)^2}\frac{1}{(1+x)^2},$$

$$R = \left(1-\frac{2}{(1+x)(1+y)}\right)^2,$$

$$A = \frac{2}{(1+y)}\frac{2x}{(1+x)^2}. \quad (10)$$

It can easily be confirmed that for $y=1$ Eq. (10) yields the same results as Eq. (7). For a case that the absorbing layer is placed on a perfect mirror, the cavity decay time into port 2 is considered infinity or, equivalently, $y=0$. The reflection and absorption coefficients at the resonant frequency are plotted in Fig. 5(b) as functions of x. In this case, the maximal absorption reaches 100% at the resonant frequency and the transmission is identically zero.

We emphasize that the analysis presented above is based on a specific assumption that must invariably be relaxed in the context of a practical solar absorber. The assumption is that the absorption bandwidth (defined as the overlap between the source bandwidth and the intrinsic absorption spectrum of the solid material) is small compared to both the cavity bandwidth, $1/\tau_{\mathrm{cav}}$, and the inverse absorption time, $1/\tau_{\mathrm{abs}}$. In the next section we consider the effects of Q_{cav} and Q_{abs} on net absorption over a finite, nonzero, range of frequencies.

IV. NUMERICAL SIMULATION OF A 2D PHOTONIC CRYSTAL FILM

In this section we present a numerical solution of Maxwell's equations in a thin-film 2D photonic crystal exhibiting absorption enhancement by parallel interface refraction. We consider a 2D photonic crystal with infinite width and finite (four unit cells) thickness, embedded in air as shown in Fig. 1(a). The radius of each rod is chosen, as before, to be $0.16a$ and the dielectric constant of the rods is 11.9. To calculate the net absorption of light by the thin-film photonic crystal, we use the finite-difference time-domain method [18]. A Bloch (periodic) boundary condition is applied in the x direction. A perfectly matched layer (PML) condition [19] is applied to absorb all light leaving the film and to terminate the computational domain in the y direction. In our simulations, the PML is applied at boundary lines $y=0$ and $y=La$, where a is the lattice constant, L is chosen (for example) to be 20, and the PC film is placed in the spatial range $y=(10-14)a$. The domain size of L and the position of the PC inside the domain do not affect the simulation results (transmission, reflection, absorption) because the PML simulates escape of light into infinite free space (no reflections from the PML back to the PC). The spatial resolution is 20 mesh points per lattice constant a $[\Delta x=\Delta y=(1/20)a]$. The temporal resolution is $(0.5/20)a/c$, where c is the light speed in vacuum.

The absorption in the thin-film photonic crystal is introduced through the conductivity σ in the Maxwell's equations {assuming the wave form $E=E_0 \exp[i(\vec{k}\cdot\vec{r}-\omega t)]$},

$$\nabla \times \mathbf{E} = i\omega\mu_0\mathbf{H}, \quad \nabla \times \mathbf{H} = (\sigma - i\omega\epsilon_r\epsilon_0)\mathbf{E}, \quad (11)$$

where ϵ_r is the relative dielectric constant and μ_0 and ϵ_0 are the permeability and permittivity of vacuum, respectively. The propagation constant k for a plane wave is given by $k^2 = \omega^2\epsilon_r\epsilon_0\mu_0+i\omega\mu_0\sigma$. In a uniform medium with $\sigma \ll \omega\epsilon_r\epsilon_0$, the propagation constant
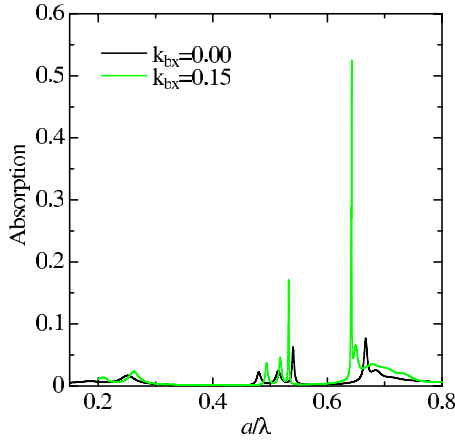
FIG. 6. (Color online) Absorption spectra of 2D photonic crystals of four unit cells thickness with $\sigma=0.02$, for normal incidence (black curve) and $k_{bx}=0.15(2\pi/a)$ [green (gray) curve].

$$k \sim \frac{\omega}{c}\sqrt{\epsilon_r} + i\frac{1}{2}\frac{\mu_0 c\sigma}{\sqrt{\epsilon_r}} \qquad (12)$$

or the wave intensity decays as $\exp[-(\mu_0 c\sigma/\sqrt{\epsilon_r})r]$, where r is the propagation distance. In what follows, the conductivity σ is expressed in units of $1/(\mu_0 ca)$. The decay length (due to absorption) is frequency independent and proportional to $\sqrt{\epsilon_r}/\sigma$. For example, $\sigma=0.01$ corresponds to a decay length of $150a$ in a uniform medium with $\epsilon_r=2.25$.

For simplicity, we assume a frequency-independent $\sigma=0.02$. First, we show in Fig. 6 a plot of total absorption by the PC film for normal incident and off-normal incident light spanning a frequency range from the first to the third photonic band. As discussed in Sec. II, the absorption enhancement for normal incident light in the frequency range of the first band ($a/\lambda \sim 0-0.26$) corresponds to conventional Fabry-Pérot resonances. In our case, the peak enhancement factor is about 3–4. For normal incident light in the second band ($a/\lambda \sim 0.48-0.54$), corresponding to "longitudinal" slow modes, the peak enhancement factor is 14. Finally, the peak absorption for off-normal incidence in the third band ($a/\lambda \sim 0.60-0.659$) with PIR exhibits a much larger enhancement factor of ~ 112.

Next, we show in Fig. 7(a) a plot of total absorption by the PC film as a function of frequency for various values of parallel-to-interface component of the incident wave vector k_{bx}. Strong enhancements of absorption are observable in specific frequency regions. The strongest peaks correspond to high-Q resonant modes induced by PIR. For $k_{bx}=0.15(2\pi/a)$, the total absorption of 54% at the peak frequency in a free-standing thin film of only four-unit-cell thickness is obtained. This exceeds the theoretical limit of single-mode cavity in mode-coupling theory. We interpret this excess absorption as arising from the interplay between nearly degenerate cavity resonances. For a uniform medium with the same average σ and same average dielectric constant, the total absorption is only 0.47%. In other words, an enhancement factor of 112 is achieved through appropriate microstructuring of the film. The normal incidence ($k_{bx}=0$)
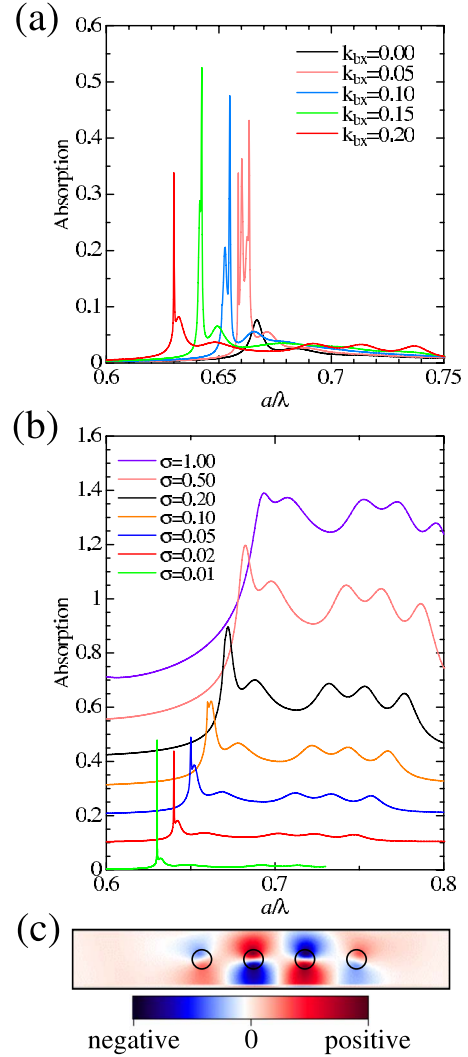

FIG. 7. (Color online) Absorption spectra of 2D photonic crystals of four unit cells thickness for (a) $\sigma=0.02$ with varied k_{bx}, (b) $k_{bx}=0.2(2\pi/a)$ with varied σ. Note that in (b) the plotted curves are shifted from the previous one (smaller σ) on the x axis by $\Delta a/\lambda=0.01$ and on the y axis by 0.1 for visual clarity. (c) Electric field distribution for $a/\lambda=0.63$, $k_{bx}=0.2(2\pi/a)$. The positions of dielectric rods are indicated by open circles.

case shows a much smaller absorption peak as expected from our picture of PIR.

Figure 7(b) shows net absorption as a function of frequency for various choices of σ, with $k_{bx}=0.2(2\pi/a)$. Interestingly, the peak absorption for $\sigma=0.01$ is actually higher than for $\sigma=0.02$. This is related to the observation from the mode-coupling theory that that there exists an optimal absorption rate for a given Q factor of the cavity mode. As σ increases, the peak at $a/\lambda=0.63$ becomes smaller and finally disappears. For larger σ, only the lower-Q-factor, non-PIR resonances at $a/\lambda=0.63314$ and 0.64820 remain. We show in Fig. 7(c) the electric field distribution of the resonant mode at $a/\lambda=0.63$. The electric field vector is perpendicular to the plane of paper.

While the high Q factor enhances the peak intensity of absorption at the resonant frequency, the absorption spectrum

has a narrow linewidth. In contrast, a low-Q cavity (e.g., a uniform absorbing layer embedded in air) exhibits low maximal absorption on resonance but the absorption spectrum is much broader. To evaluate the efficacy of the PC film for solar-energy harvesting, we must consider an integral of the energy absorbed over a range of frequencies and over a range of incident angles.

In the artificial case that the absorption coefficient σ is frequency independent, the absorption coefficient $A \equiv (1 - T - R)$ for the free-standing dielectric slab exhibits the frequency dependence

$$A(\omega) = \frac{2 \dfrac{1}{2\tau_{\text{cav}}} \dfrac{1}{2\tau_{\text{abs}}}}{\left(\dfrac{1}{2\tau_{\text{cav}}} + \dfrac{1}{2\tau_{\text{abs}}} \right)^2 + (\omega - \omega_0)^2}. \quad (13)$$

Integration over the entire frequency space yields a total absorption of $\pi / (\tau_{\text{cav}} + \tau_{\text{abs}})$. Therefore, for a given absorption rate τ_{abs} (or σ), smaller Q_{cav} yields more total absorption integrated over *all* frequencies. In practice, absorption is present for only a finite range of frequencies. Also the relevant source of light (say the sun) has dominant emission in a specific frequency range. It is then advantageous to employ high-Q cavities that maximize net absorption in the spectral range defined by the overlap of the source spectrum and the thin-film absorption spectrum. Below, we introduce a simple model to analyze net absorption of light in a photonic crystal film within a finite spectral range.

Consider a thin film with a fixed resonant frequency ω_0, with a fixed rate of intrinsic absorption σ_0, and a variable cavity quality factor Q_{cav} determined by the nature of its periodic microstructure. For simplicity, assume that the relevant spectral range is incorporated by choosing the frequency-dependent conductivity function

$$\sigma(\omega) = \begin{cases} \sigma_0 & \text{for } |\omega - \omega_0| < \omega_0 / Q_{\text{range}}, \\ 0 & \text{otherwise}. \end{cases} \quad (14)$$

Here we associate the quality factor Q_{range} with the relevant spectral range. We assume that the absorption of light by the film as a function of frequency is described by the mode coupling theory, and that the total absorption (figure of merit) is simply the integral of A [given in Eq. (13)] over the frequency window of $\sigma(\omega)$ above. Using the above assumption, we find that for low absorption ($Q_{\text{abs}} \geqslant Q_{\text{cav}}$) the total absorption can be largely enhanced by employing a high-Q cavity. For illustrative purposes, we assume $Q_{\text{abs}} = Q_{\text{range}} = 3000$ and calculate the total absorption for various Q_{cav}. We then compare the total absorption for various choices of Q_{cav} with the case that $Q_{\text{cav}} = 10$ (corresponding to the Fabry-Pérot resonance of a homogeneous thin film). As shown in Fig. 8(a), the total absorption enhancement factor is as large as 70 provided that the uniform film ($Q_{\text{cav}} = 10$) is replaced by a microstructured film with cavity quality factor that matches the intrinsic absorption quality factor. We also consider the case where the relevant spectral range is wider than the linewidth of cavity mode. We assume $Q_{\text{abs}} = Q_{\text{cav}} = 3000$ and calculate the total absorption for various Q_{range}. The results are compared with the case that $Q_{\text{abs}} = 3000$, $Q_{\text{cav}} = 10$ and plotted
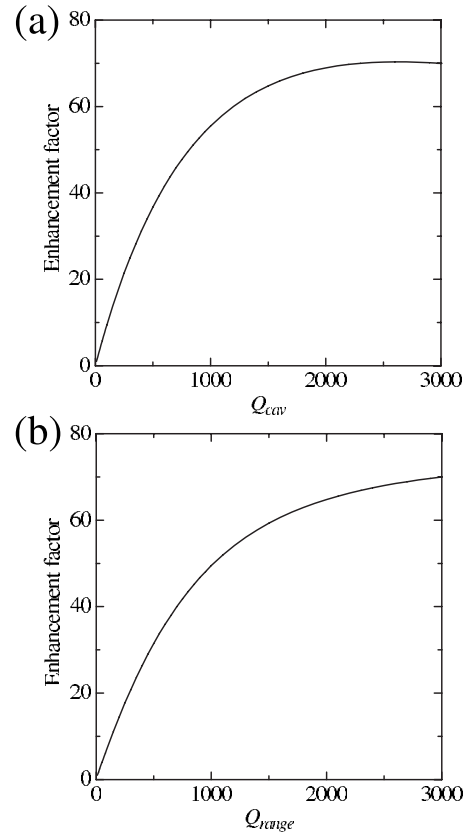

FIG. 8. (a) Enhancement factor of total absorption as a function of Q_{cav} for $Q_{\text{abs}} = Q_{\text{range}} = 3000$ compared to the case of $Q_{\text{cav}} = 10$. (b) Enhancement factor of total absorption as a function of Q_{range} for $Q_{\text{abs}} = Q_{\text{cav}} = 3000$ compared to the case of $Q_{\text{abs}} = 3000$, $Q_{\text{cav}} = 10$.

in Fig. 8(b). The enhancement factor decreases with decreasing Q_{range} (wider relevant spectral range), consistent with the above discussion.

Finally, we evaluate the total absorption over a range of incident angles for the 2D PC structure with thickness of four unit cells using FDTD simulation. The total absorption is evaluated by integrating the absorption shown in Fig. 7(a) over a spectral range of the third band ($a/\lambda = 0.58 - 0.68$) and over an angular range of $\theta = 0° - 20°$. This enlarged spectral range is used to capture the various PIR resonances spanned by the angular range. The total absorption in the microstructured film is then compared to that of a uniform film of the same thickness with the same average σ and the same average dielectric constant. An overall enhancement factor of about 5 in the total absorption of light incident within the cone of incident angles and the relevant spectral range is obtained as a result of microstructuring the film. The enhancement factor is reduced from a factor of 70 to a factor of 5 because the relevant spectral range ($a/\lambda = 0.58 - 0.68$), corresponding to $Q_{\text{range}} = 12.6$, is far wider than the linewidth of PIR resonance, similar to the situation in Fig. 8(b).

Our numerical studies demonstrate that PIR enhances absorption significantly relative to that of unstructured films. The mode-coupling model also explains why in some cases, increasing the absorption rate, beyond that allowed by the cavity Q factor, leads to a smaller net absorption at the resonant peak. The absorption enhancement factor becomes

smaller when one includes a wider range of frequencies. For $Q_{range}=\infty$, it was shown that in a free-standing film the optimum absorption occurs when $Q_{cav}=Q_{abs}$. For $Q_{range}=0$, it is best to set $Q_{cav}=0$. Therefore, it is expected that for a finite Q_{range} the optimal Q_{cav} is somewhere between 0 and Q_{abs}. While it is advantageous to use a single-mode cavity to enhance absorption if the relevant spectral range is small, it is useful to employ many resonant modes with lower quality factors for absorption enhancement over a broad band. This arises naturally if the PC film is not perfectly periodic, but has small amounts of random disorder. This is the subject of the next section.

V. ABSORPTION BROADENING DUE TO STRUCTURAL DISORDER

For practical applications, it is important to examine the robustness of the PIR effect to small changes in the geometry of the structures. In this section, we study the effect of structural disorder on total absorption of light in the square lattice photonic crystal thin film. Random variations in structure are introduced using a 10×4 supercell. We use a FDTD computational domain with a size of $10a$ in the x direction. A periodic boundary condition is applied in the x direction and a PML condition is applied to the y direction, as described in Sec. IV. A simple model for structural disorder consists of small random variations in the radius r of dielectric rods. Dielectric rods with randomly varying radii ranging from $r=0.155a$ to $0.165a$ are distributed in the supercell. The probability distribution of rod radii is chosen to be uniform over the interval $(0.155, 0.165)a$.

Figure 9(a) shows absorption spectra for four different realizations of free-standing disordered photonic crystal thin films. The incident plane wave is chosen with lateral wave vector $k_{bx}=0.2(2\pi/a)$. The intrinsic absorption coefficient of each dielectric rod defined by $\sigma=0.02$ is chosen to be frequency independent. The absorption spectrum for a perfect structures is also shown for comparison (dotted line). Clearly, one effect of disorder is the reduction of the quality factor of the PIR-induced cavity. However, disorder creates additional resonant modes at other frequencies not present in the perfectly ordered structures. When the relevant spectral range is broad (e.g., $a/\lambda=0.6-0.7$), the total absorption in the disordered thin film photonic crystal is larger than for the perfect photonic crystal film. Such a broad spectral range may be relevant to solar-energy harvesting. However, for a narrow relevant spectral range, a high-Q cavity is valuable to obtain strong absorption at specific resonant frequencies. High quality factors are achieved by suppressing structural disorder as well as by using a thicker photonic crystal film. We demonstrate this by calculating absorption spectra for disordered photonic crystal film thickness of eight unit cells. The results for four different realizations of disordered structures are shown in Fig. 9(b). In general, the peaks in Fig. 9(b) are sharper and the maximal absorptions near the original resonant frequency ($a/\lambda=0.63$) are larger than those in Fig. 9(a).

VI. PARALLEL INTERFACE REFRACTION IN 3D CUBIC PHOTONIC CRYSTALS

In this section, we demonstrate the PIR effect in suitably structured 3D photonic crystal films. As discussed earlier,
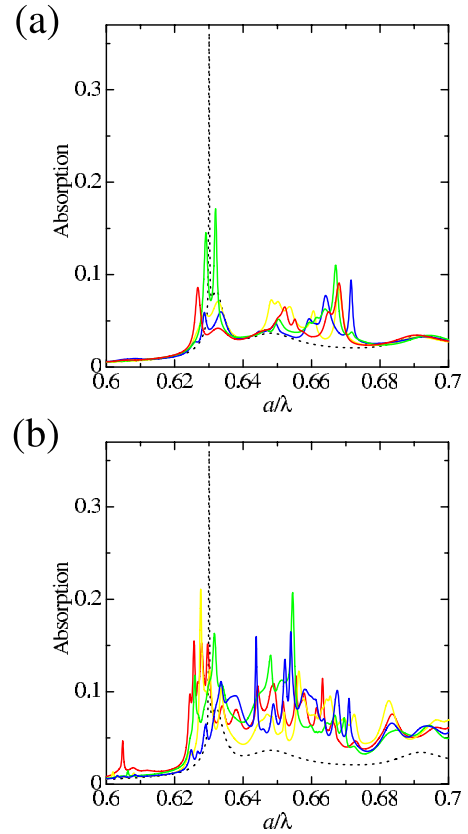

FIG. 9. (Color online) Absorption spectra for disordered photonic crystals with thickness of (a) four and (b) eight unit cells. The radius of dielectric rods is varied from $0.16a$ by up to $\pm0.005a$. Absorption spectra for a perfectly ordered photonic crystal of four unit cells thickness is also shown as dotted lines for comparison.

photonic crystals with cubic symmetry are well suited for achieving the PIR over a broad range of incident angles. A specific realization of such photonic crystals is in recently synthesized 3D macroporous silicon created by photoelectrochemically etching pores into silicon [20]. A schematic of this cubic-symmetric PC is shown in Fig. 10. The structure is fabricated first, starting from a square lattice of shallow cir-
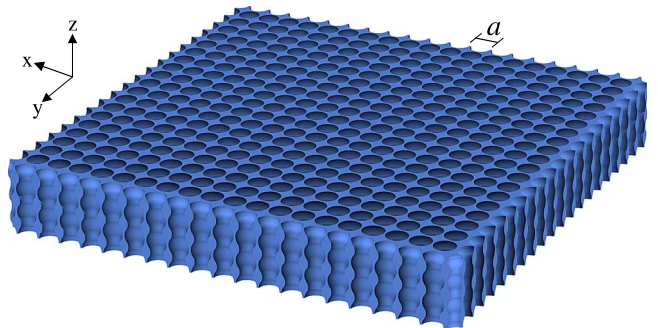

FIG. 10. (Color online) Schematic for macroporous 3D photonic crystals created by photoelectrochemical etching. The structure consists of a square lattice of deep pores with the radius periodically modulated along the vertical direction. The structure has a cubic lattice symmetry when a lattice constant in the vertical direction is chosen to be the same as that in the x-y plane.
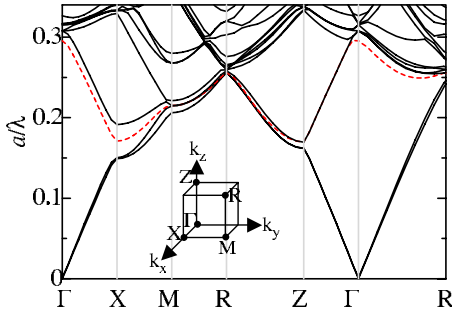
FIG. 11. (Color online) Band diagram for the 3D macroporous silicon photonic crystal shown in Fig. 10. The radius r of pores is assumed to be sinusoidally modulated along the z direction, with an explicit form $r=[0.25-0.05\cos(2\pi z/a)]a$, where z is the vertical position, and a is the lattice constant for the x and y directions. The dielectric constant for silicon is 11.9. The third band is marked by a broken red (dark gray) line. The inset shows the first Brillouin zone and high-symmetry points at the zone boundary.

cular etch pits on a silicon wafer. Subsequently, by applying a photoelectrochemical etch process, deep pores are created along the vertical direction from each etch pit. During the etch process, the radius of the pores is modulated by changing the intensity of illumination being applied. The final structure obtained has a cubic lattice symmetry when a lattice constant in the vertical direction is chosen to be the same as that in the x-y plane.

For illustration, we consider a 3D macroporous silicon PC film with infinite size in the lateral directions and three unit cells in thickness. The radius r of pores is assumed to be sinusoidally modulated along the z direction, with an explicit form $r=[0.25-0.05\cos(2\pi z/a)]a$, where z is the vertical position. The corresponding band diagram is shown in Fig. 11. We consider the third band [marked by the broken red (dark gray) line in Fig. 11]. For an incident plane wave with $a/\lambda=0.253$, the Bloch modes inside the 3D PC with the matching frequency is represented by an isofrequency surface (in the k space) shown in Fig. 12 [cubiclike shape, centered at (0,0,0)]. The sphere [also centered at (0,0,0)] represents all possible wave vectors that can be taken by an incident plane wave with $a/\lambda=0.253$.

Consider an incident plane wave on a PC with interfaces parallel to the x-y plane. Suppose that the incoming light makes an incident angle $\theta=54.6°$ relative to the surface normal and an azimuthal angle $\phi=14°$ relative to the $+x$ axis. This corresponds to a lateral wave vector $(k_x, k_y) = (0.2, 0.05)(2\pi/a)$ shown by the blue (dark gray) arrow. Similarly to the previous analysis in 2D cases, the Bloch mode that can be excited inside PC's must possess the same lateral wave vector and the same frequency. This corresponds to a Bloch mode at the beginning of the red (gray) arrow. The propagation direction of this Bloch mode, however, is given by the direction of the group velocity at this Bloch vector. This is equivalent to the isofrequency surface normal and is indicated by the red (gray) arrow. Figure 13(a) shows a top view of the same picture as Fig. 12. Due to the "flatness" of the isofrequency surface, the direction of the group velocity is nearly parallel to the air/PC interfaces and the PIR phenomenon can be expected for this incident plane wave.
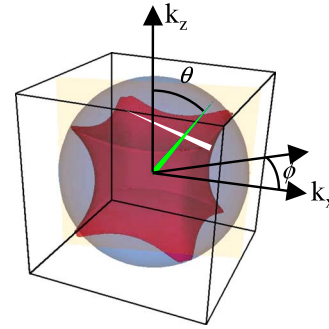

FIG. 12. (Color online) Isofrequency surface of the third band at $a/\lambda=0.253$ for the 3D photonic crystals depicted in Fig. 10 (cubiclike shape) and isofrequency surface for an incident plane wave at the same a/λ (sphere). Both surfaces reside in the reciprocal space (k_x, k_y, k_z) and are centered at (0,0,0). The green (gray) arrow indicates the wave vector of the incident plane wave with an incident angle $\theta=54.6°$ and an azimuthal angle $\phi=14°$, corresponding to a lateral wave vector $(k_x, k_y)=(0.2, 0.05)(2\pi/a)$. The white arrow indicates the propagation direction for the Bloch mode excited in the PC where it is nearly parallel to the air/PC interfaces.

Furthermore, the cubic shape of isofrequency surface suggests that the PIR can be obtained for a wide range of incident angles ϕ and θ. For instance, the direction of group velocity for the incident azimuthal angles $\phi=66°$ and $\phi=270°$ also indicates the PIR as shown in Figs. 13(b) and 13(c), respectively.

We calculate the transmission spectrum for an incident plane wave with electric field in the plane of incidence (P polarized) and lateral wave vector $(\vec{k}_{bx}, \vec{k}_{by}) = (0, -0.2)(2\pi/a)$, for the case of $\sigma=0$ (no absorption) by 3D FDTD. As before, the dielectric constant assumed for silicon is 11.9. The spatial resolution is ten mesh points per lattice constant a [$\Delta x=\Delta y=\Delta z=(1/10)a$]. The temporal resolution is $(0.5/10)a/c$, where c is the light speed in vacuum. The result is shown in Fig. 14. The transmission spectrum exhibits strong resonances at $a/\lambda=0.253$ and 0.269. In Fig. 14, we have chosen three unit cells for the thickness of the photonic crystal film such that one Fabry-Pérot resonance corresponds to the Bloch vector $\vec{k}_b=(0, -0.2, 1/3)(2\pi/a)$ (see Appendix A). This is the Bloch mode indicated by the tip of the blue (dark gray) arrow in Fig. 13(c), showing the PIR at $a/\lambda=0.253$. Hence, we attribute the strong resonance at $a/\lambda=0.253$ in Fig. 14 to the PIR from band 3. Unlike the simpler case of a 2D PC with only one band at the PIR resonant frequency, for the 3D photonic crystal there are five bands (bands 1–5) that intersect the line $a/\lambda=0.253$. However, the possibility of the sharp peak at $a/\lambda=0.253$ being from other bands is excluded since the other bands do not possess the corresponding Fabry-Pérot resonant Bloch vectors at this frequency. A similar consideration reveals that the second sharp peak at $a/\lambda=0.269$ is the result of PIR from band 4. The refraction for most incident angles is strongly negative (parallel to the interface) and usually out of the plane of incidence. The shape of the isofrequency surface suggests that PIR can be obtained for at least a 50° cone of incoming, off-normal angles and a bandwidth of ~15% of the center frequency for band 3.
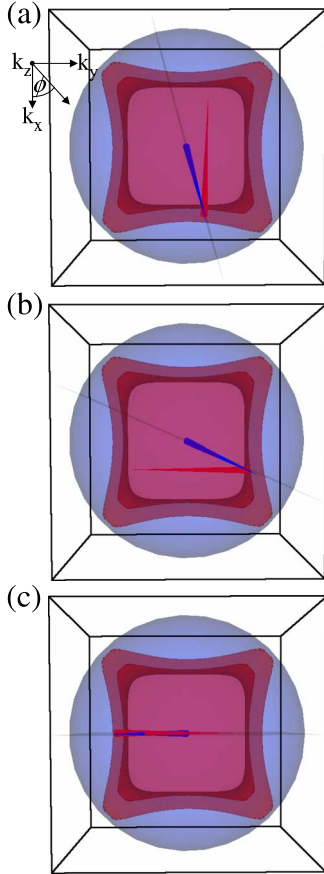
FIG. 13. (Color online) Top view of isofrequency surfaces shown in Fig. 12. In (a), the blue (dark gray) arrow indicates the wave vector of the incident plane wave with an incident angle $\theta = 54.6°$ and an azimuthal angle $\phi = 14°$, corresponding to a lateral wave vector $(k_x, k_y) = (0.2, 0.05)(2\pi/a)$. The red (gray) arrow indicates the propagation of direction for the Bloch mode excited in the PC where it is nearly parallel to the air/PC interfaces (same as Fig. 12). In (b) and (c), the blue (dark gray) arrows correspond to $\phi = 66°$ and $\phi = 270°$. Again, the PIR is observed.

Finally, we show in Fig. 15 the absorption spectra calculated by 3D FDTD for $\sigma = 0.01$, 0.02, and 0.05. Within the plotted frequency range $a/\lambda = 0.24 - 0.28$, the fixed lateral Bloch vector $(k_{bx}, k_{by}) = (0, -0.2)(2\pi/a)$ corresponds to a range of incident angle $\theta = 56.4° - 45.6°$. Comparing to a uniform layer with the same average σ and same average dielectric constant, the absorption at $a/\lambda = 0.253$ for $\sigma = 0.01$ is enhanced by a factor of ~ 55 at the resonant frequency. Again, we observe an optimal absorption rate ($\sigma = 0.02$) for the maximal net absorption in this case. In general, a fixed absorption rate σ is given for a certain material. The maximal net absorption in the free-standing film can then be obtained adjusting structural parameters such as dielectric filling fraction or photonic crystal thickness so that Q_{cav} and Q_{abs} are suitably matched. Here again it is advantageous to replace the free-standing PC film with one placed on a substrate consisting of a PC back reflector [21,22], in order to increase the net absorption on resonance. For a broadband light source such as the sun, it is also advantageous to introduce some disorder into the film to create a broader spectrum
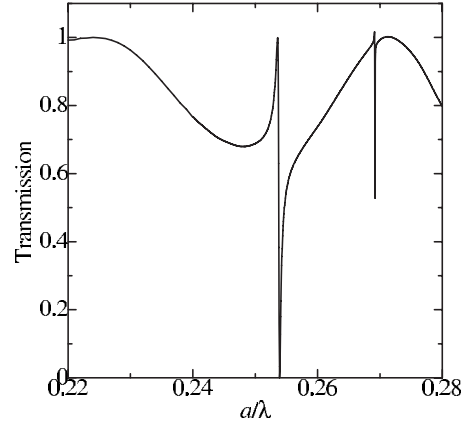

FIG. 14. Transmission spectra calculated by 3D FDTD for a photoelectrochemically etched 3D photonic crystal with thickness of three unit cells. An incident plane wave possesses a lateral wave vector $(k_x, k_y) = (0, -0.2)(2\pi/a)$. A strong resonant peak due to the PIR effect is observed at $a/\lambda \sim 0.253$.

of resonances of lower-quality-factor resonances for each incident angle. The very large (50°) acceptance cone for the PIR effect in this cubic crystal may be particularly useful for capturing both direct sunlight and diffusely scattered light impinging on the film.

VII. CONCLUSION

We have presented a theoretical analysis of parallel interface refraction in 2D and 3D photonic crystals. In particular, we showed that for certain cases a light beam incident on a thin-film photonic crystal can couple through acute negative and/or out-of-plane refraction to Bloch modes whose direction of propagation is nearly parallel to the surfaces of the photonic crystal. In such cases, it takes a very long time
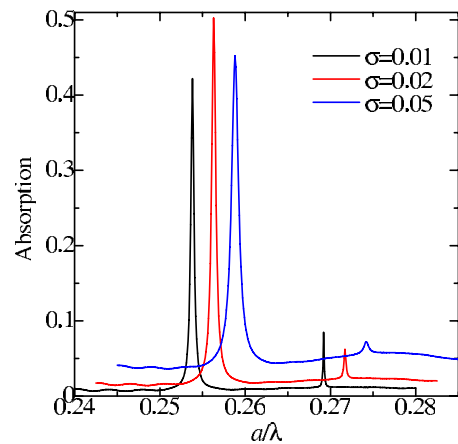

FIG. 15. (Color online) Absorption spectra of 3D photonic crystals with thickness of three unit cells for the lateral Bloch vector $(k_{bx}, k_{by}) = (0, -0.2)(2\pi/a)$ with various choices of σ. Within the frequency range $a/\lambda = 0.24 - 0.28$, the fixed lateral Bloch vector corresponds to a range of incident angle $\theta = 56.4° - 45.6°$. The plotted curves are each shifted from the previous one (smaller σ) on the x axis by $\Delta a/\lambda = 0.0025$ for visual clarity.

before the light beam exits the thin film and the optical resonances can be much stronger than those of other previously reported slow-group-velocity effects. The parallel interface refraction effect relies on the "flatness" of isofrequency lines (2D) or surfaces (3D) of certain photonic bands. From this viewpoint, we have focused on square (2D) and cubic lattice (3D) photonic crystals, as they tend to exhibit more "flat" dispersion than other types of lattice. For the 3D cubic PC films synthesized by modulated-pore electrochemical etching, the PIR effect may appear over a bandwidth of roughly 15% relative to the center frequency and over an acceptance cone of incident angles of about 50°. We demonstrated the use of a parallel-interface-refraction-induced high-Q cavity in thin-film photonic crystals to enhance absorption. For the purpose of interpretation, we have developed a simple model based on the temporal mode-coupling theory. It is shown that the total amount of absorption is not proportional to the Q factor of the cavity but there exist optimal values for maximal absorption. For a symmetric cavity with only one resonant mode, the maximum absorption of 50% is obtained when $Q_{abs}=Q_{cav}$. By introducing a highly reflective substrate such as a PC back reflector, the net absorption can be increased well above 50%. Numerical results calculated by FDTD show a good qualitative agreement with the mode-coupling analysis. Finally, the effects of fabrication-related structural disorders are discussed. It is found that for absorbers with a narrow linewidth, precise fabrication or a thick photonic crystal structure is necessary to obtain strong absorption. However, for broadband light sources and absorbers, additional resonant modes caused by weak disorder can actually serve to improve the total absorption of light. Since the solar spectrum spans a very wide spectral range, naturally occurring disorder in the photonic crystal film fabrication may in fact improve solar-energy harvesting. One specific application of PIR-enhanced solar energy harvesting is to the widely studied Grätzel cells [23] consisting of a TiO$_2$ backbone photonic crystal, in which an electrolyte fills the interior void regions of the periodic microstructure, and a transparent electrode is placed on the top surface of the absorbing film. Applications to silicon-based solar cells may also be possible, provided that a suitable p-n junction [24] and electrodes can be incorporated with a periodically structured active region.

APPENDIX A: PHYSICAL INTERPRETATION FOR RESONANT PEAKS IN FINITE-THICKNESS PHOTONIC CRYSTALS

In a conventional Fabry-Pérot resonator, the resonant condition is that an integer number m of half wavelengths in vacuum, λ_0, is equal to the cavity length d multiplied by the refractive index of the cavity, n, or $m\lambda_0/2=nd$. This can be rewritten as a condition for the wave vector in vacuum $k_0 \equiv 2\pi/\lambda_0$ as $nk_0=m\pi/d$. In a PC with finite thickness, the Fabry-Pérot resonant condition takes the same form except that the term nk_0 is replaced by the longitudinal Bloch vector. For example, in Fig. 3 with $d=4a$, the resonant condition corresponds to modes with longitudinal Bloch vectors k_{by} equal to $(1/4,2/4,3/4)(\pi/a)$. Specifically, for a lateral Bloch vector $k_{bx}=0.2(2\pi/a)$, the dimensionless frequencies calculated by the plane-wave expansion method for these three longitudinal Bloch vectors are $a/\lambda=0.649\,46$, 0.633 77, and 0.632 61, respectively. These roughly agree with the positions of peaks in the solid curve in Fig. 3(b), which are $a/\lambda=0.648\,20$, 0.633 14, and 0.630 00, respectively. The small discrepancy may be attributed to the Bloch vector uncertainty associated with a structure of finite thickness. Further agreement is obtained when we consider the group velocity v_g, and the angle of refraction θ (measured relative to the surface normal). The smaller longitudinal group velocity obtained by the plane wave expansion method indeed corresponds the sharper resonant peak in Fig. 3(b). For the three Bloch modes, $(v_g,\theta)=(0.172\,83c,-11.1°)$, $(0.188\,90c,-69.4°)$, $(0.260\,01c,-83.5°)$, respectively, where c is the light speed in vacuum. These correspond to the longitudinal group velocity of $0.169c$, $0.066c$, and $0.029c$, respectively. It should be pointed out that, for the first two Bloch modes, the longitudinal group velocity derived from Fig. 3(b) points to the backward direction and therefore these not excited. However, due to symmetry there exist another two Bloch modes at $(0.2,-1/4)(2\pi/a)$ and $(0.2,-2/4)(2\pi/a)$ with the same a/λ that exhibit group velocity in the forward direction and these two modes are excited instead. Similar agreement is also obtained for other cases, e.g., the first, second, and fourth bands for normal incidence shown in Fig. 3(a). Explicitly, in Fig. 3(a), the positions of peaks are, from low to high frequencies, a/λ =0.175 60, 0.245 20, 0.480 40, 0.514 00, 0.540 20, 0.668 00, 0.689 20, 0.725 20. This is comparable to the corresponding Bloch modes from the band structure: $a/\lambda=0.175\,38$, 0.245 20, 0.482 05, 0.515 65, 0.541 37, 0.671 71, 0.691 32, 0.723 95.

APPENDIX B: RANGE OF VALIDITY OF MODE COUPLING THEORY

In this appendix, we provide a detailed comparison between the mode-coupling theory and the exact solution of Maxwell's equation for optical absorption in a simple homogeneous slab resonator. While our mode-coupling model result is derived for a cavity with single resonant mode, the slab resonator exhibits a ladder of Fabry-Pérot resonances defined by the condition $nk_0d=m\pi$. Nevertheless, we find very good agreement between the two methods with respect to the relevant cavity mode. The discrepancy becomes noticeable only when the influence of the adjacent Fabry-Pérot modes is not negligible. This occurs when (1) the frequency separation between two adjacent Fabry-Pérot modes (free spectral range) is small or (2) the intrinsic absorption rate is large.

We consider light incident normally on a slab of uniform dielectric material with a refractive index n embedded in air, similar to the one shown in Fig. 4. This corresponds to a symmetric cavity with two ports in mode-coupling theory. For a dielectric slab with thickness d, the free spectral range is given by $c/2nd$, where c is the light speed in vacuum. In order to eliminate multiple Fabry-Pérot modes in the frequency range of interest, we consider a hypothetical refractive index $n=0.01$ for the dielectric slab.

The transmission coefficient for slab resonators is given by [25]

$$T = \frac{(1-R)^2}{(1-R)^2 + 4R\,sin^2(\delta/2)},$$

where $R=(1-n)^2/(1+n)^2$ is the reflection coefficient at the air/dielectric interface and $\delta=4\pi nd/\lambda_0$, λ_0 is the wavelength in vacuum. For $\sin(\delta/2) \sim \delta/2$, the full width at half maximum (FWHM) for resonant peaks, $\Delta\omega$ (the same for all resonant modes), is equal to

$$\Delta\omega = \frac{c}{nd}\frac{1-R}{\sqrt{R}}.$$

For an optical cavity with energy decaying as $\exp(-t/\tau)$, the Lorentzian line shape has FWHM $\sim 1/\tau$. Assuming the transmission line shape of the slab resonator is Lorentzian, the above FWHM gives a cavity decay time (for amplitude) τ_{FP}

$$\tau_{FP} = 2n\frac{\sqrt{R}}{1-R}\frac{d}{c}.$$

In our case, $\tau_{FP}=0.499\,95d/c$. On the other hand, the absorption decay time τ_{abs} (defined as the time scale on which the amplitude of a plane wave in the medium decays to $1/e$ of its original value), for a uniform medium (no cavity) with conductivity σ, can be found by dividing the absorption length $d_{abs}=2n/(\mu_0 c\sigma)$ [obtained from Eq. (12)] by the light speed in the dielectric material c/n. The absorption decay time τ_{abs} is then equal to $(2n^2)/(\mu_0 c^2\sigma)$. Similarly to the previous sections, we express the conductivity σ in units of $1/(\mu_0 cd)$. Then

$$\tau_{abs} = \frac{2n^2}{\sigma}\frac{d}{c},$$
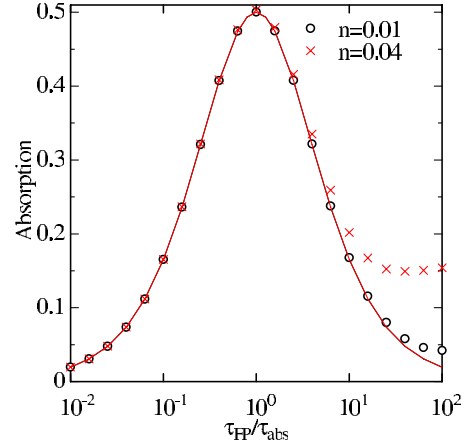
where σ is now dimensionless.

FIG. 16. (Color online) Peak absorption of a Fabry-Pérot mode in a thin slab of dielectric obtained by mode-coupling theory (solid line) and exact solution for refractive index $n=0.01$ (open circles) and $n=0.04$ ($\times$).

We calculate the absorption at the resonant frequency using the above analytic expressions for τ_{FP} and τ_{abs} in the mode-coupling analysis and show the results in Fig. 16 (solid line). We also obtain an exact solution of Maxwell's equation for the slabs by assuming two counterpropagating plane waves in each of the three regions [air, absorbing dielectric, air (see Fig. 4)] and matching the electric field and its derivative at each boundary. The exact absorption coefficients obtained are plotted as open circles and $\times$'s in Fig. 16. The mode-coupling theory agrees very well with the exact solution when the absorption rate is small but is less accurate when the absorption rate is large. This is because, when the Q factors of the cavity are reduced by absorption, the effects from the adjacent Fabry-Pérot modes are no longer negligible. Alternatively, a small frequency separation between Fabry-Pérot resonances also leads to deviation from the exact solution. To illustrate this point, we show the mode-coupling results and exact results for a second case with the refractive index $n=0.04$. The two sets of results are shown as the (red) solid line and $\times$, respectively, in Fig. 16. With other structural parameters the same, the cavity decay time τ_{FP} is $0.4992d/c$, roughly the same as before. However, the frequency separation between two adjacent Fabry-Pérot modes is four times smaller. In this case, the discrepancy between the mode-coupling theory and the exact result is considerable for large τ_{FP}/τ_{abs}.

[1] S. John, Phys. Rev. Lett. **53**, 2169 (1984).

[2] S. John, Phys. Rev. Lett. **58**, 2486 (1987).

[3] E. Yablonovitch, Phys. Rev. Lett. **58**, 2059 (1987).

[4] S. Y. Lin, V. M. Hietala, L. Wang, and E. D. Jones, Opt. Lett. **21**, 1771 (1996).

[5] H. Kosaka, T. Kawashima, A. Tomita, M. Notomi, T. Tamamura, T. Sato, and S. Kawakami, Phys. Rev. B **58**, R10096 (1998).

[6] H. Kosaka, T. Kawashima, A. Tomita, M. Notomi, T. Tamamura, T. Sato, and S. Kawakami, Appl. Phys. Lett. **74**, 1212 (1999).

[7] M. Notomi, Phys. Rev. B **62**, 10696 (2000).

[8] J. B. Pendry, Phys. Rev. Lett. **85**, 3966 (2000).

[9] T. Prasad, V. Colvin, and D. Mittleman, Phys. Rev. B **67**, 165103 (2003).

[10] R. Brendel, *Thin-Film Crystalline Silicon Solar Cells: Physics*

and Technology (Wiley-VCH, Weinheim, 2003).

[11] H. A. Haus, *Waves and Fields in Optoelectronics* (Prentice-Hall, Englewood Cliffs, NJ, 1984).

[12] J. P. Dowling, M. Scalora, M. J. Bloemer, and C. M. Bowden, J. Appl. Phys. **75**, 1896 (1994).

[13] K. Sakoda, Opt. Express **4**, 167 (1999).

[14] U. Fano, Phys. Rev. **124**, 1866 (1961).

[15] S. Fan and J. D. Joannopoulos, Phys. Rev. B **65**, 235112 (2002).

[16] A. Chutinan and S. John (unpublished).

[17] C. Manolatou, M. J. Khan, S. Fan, P. R. Villeneuve, H. A. Haus, and J. D. Joannopoulos, IEEE J. Quantum Electron. **35**, 1322 (1999).

[18] K. S. Yee, IEEE Trans. Antennas Propag. **14**, 302 (1966).

[19] J. P. Berenger, J. Comput. Phys. **114**, 185 (1994).

[20] J. Schilling, F. Müller, S. Matthias, R. B. Wehrspohn, U. Gösele, and K. Busch, Appl. Phys. Lett. **78**, 1180 (2001).

[21] P. G. O'Brien, N. P. Kherani, S. Zukotynski, G. A. Ozin, E. Vekris, N. Tetreault, A. Chutinan, S. John, A. Mihi, and H. Míguez, Adv. Mater. (Weinheim, Ger.) **19**, 4177 (2007).

[22] A. Mihi, H. Míguez, I. Rodríguez, S. Rubio, and F. Meseguer, Phys. Rev. B **71**, 125131 (2005).

[23] M. Grätzel, Nature (London) **414**, 338 (2001).

[24] G. P. Smestad, *Optoelectronics of Solar Cells* (SPIE Press, Bellingham, WA, 2002).

[25] G. Hernandez, *Fabry-Pérot Interferometers* (Cambridge University Press, Cambridge, U.K., 1986).